

DES meets Gaia: discovery of strongly lensed quasars from a multiplet search

A. Agnello^{1*}, H. Lin², N. Kuropatkin², E. Buckley-Geer², T. Anguita³, P.L. Schechter⁴, T. Morishita⁵, V. Motta⁶, K. Rojas⁶, T. Treu^{5,†}, A. Amara⁷, M.W. Auger⁸, F. Courbin⁹, C.D. Fassnacht¹⁰, J. Frieman², A. More¹¹, P.J. Marshall¹², R.G. McMahon^{8,13}, G. Meylan⁹, S.H. Suyu¹⁴, K. Glazebrook¹⁵, N. Morgan¹⁶, B. Nord², T. M. C. Abbott¹⁷, F. B. Abdalla^{18,19}, J. Annis², K. Bechtol², A. Benoit-Lévy^{18,20,21}, E. Bertin^{20,21}, R. A. Bernstein²², D. Brooks¹⁸, D. L. Burke^{23,12}, A. Carnero Rosell^{24,25}, J. Carretero²⁶, C. E. Cunha¹², C. B. D’Andrea²⁷, L. N. da Costa^{24,25}, S. Desai²⁸, A. Drlica-Wagner², T. F. Eifler^{29,30}, B. Flaugher², J. García-Bellido³¹, E. Gaztanaga³², D. W. Gerdes^{33,34}, D. Gruen^{12,35}, R. A. Gruendl^{36,37}, J. Gschwend^{24,25}, G. Gutierrez², K. Honscheid^{38,39}, D. J. James⁴⁰, K. Kuehn⁴¹, O. Lahav¹⁸, M. Lima^{24,25,42}, M. A. G. Maia^{24,25}, M. March²⁷, F. Menanteau^{36,37}, R. Miquel^{26,43}, R. L. C. Ogando^{24,25}, A. A. Plazas²⁹, E. Sanchez⁴⁴, V. Scarpine², R. Schindler³⁵, M. Schubnell³³, I. Sevilla-Noarbe⁴⁴, M. Smith⁴⁵, M. Soares-Santos², F. Sobreira^{24,46}, E. Suchyta⁴⁷, M. E. C. Swanson³⁷, G. Tarle³³, D. Tucker², R. Wechsler²³

¹European Southern Observatory, Karl-Schwarzschild-Strasse 2, 85748 Garching bei München, DE

²Fermi National Accelerator Laboratory, Batavia, IL 60510

³Departamento de Ciencias Físicas, Universidad Andres Bello Fernandez Concha 700, Las Condes, Santiago, Chile

⁴MIT Kavli Institute for Astrophysics and Space Research, 37-664G, 77 Massachusetts Avenue, Cambridge, MA 02139

⁵Department of Physics and Astronomy, PAB, 430 Portola Plaza, Box 951547, Los Angeles, CA 90095-1547, USA

⁶Instituto de Física y Astronomía, Universidad de Valparaíso, Avda. Gran Bretaña 1111, Playa Ancha, Valparaíso 2360102, Chile

^{7–51} Full list of affiliations at the end of the paper.

† Packard Fellow.

This paper includes data gathered with the 6.5 meter Magellan Telescopes located at Las Campanas Observatory, Chile.

Accepted . Received

ABSTRACT

We report the discovery, spectroscopic confirmation and first lens models of the first two, strongly lensed quasars from a combined search in WISE and Gaia over the DES footprint. The four-image lens WGD2038-4008 (r.a.=20:38:02.65, dec.=−40:08:14.64) has source- and lens-redshifts $z_s = 0.777 \pm 0.001$ and $z_l = 0.230 \pm 0.002$ respectively. Its deflector has effective radius $R_{\text{eff}} \approx 3.4''$, stellar mass $\log(M_*/M_\odot) = 11.64^{+0.20}_{-0.43}$, and shows extended isophotal shape variation. Simple lens models yield Einstein radii $R_E = (1.30 \pm 0.04)''$, axis ratio $q = 0.75 \pm 0.1$ (compatible with that of the starlight) and considerable shear-ellipticity degeneracies. The two-image lens WGD2021-4115 (r.a.=20:21:39.45, dec.=−41:15:57.11) has $z_s = 1.390 \pm 0.001$ and $z_l = 0.335 \pm 0.002$, and Einstein radius $R_E = (1.1 \pm 0.1)''$, but higher-resolution imaging is needed to accurately separate the deflector and faint quasar image. We also show high-rank candidate doubles selected this way, some of which have been independently identified with different techniques, and discuss a DES+WISE quasar multiplet selection.

Key words: gravitational lensing: strong – methods: statistical – astronomical data bases: surveys – techniques: image processing

1 INTRODUCTION

Strong gravitational lensing by galaxies relies on the alignment of a (typically massive) galaxy with a more distant source. In the case of lensed quasars, this enables multiple lines of investigation, such as: the deflector mass and density profile, in both luminous and dark matter (e.g. Bate et al. 2011; Oguri et al. 2014; Schechter et al. 2014); a super-resolved study of distant sources, thanks to magnification (Peng et al. 2006; Ding et al. 2017) and micro-lensing by individual stars in the deflector (Sluse et al. 2012; Hutsemékers et al. 2015; Motta et al. 2017); an unbiased census of dark and baryonic substructure around the deflector (Mao & Schneider 1998; Dalal & Kochanek 2002; Gilman et al. 2017; Hsueh et al. 2017); and the measurement of cosmological distances, from delays between different light-curves (Refsdal 1964; Suyu et al. 2017). All these investigations are currently limited by sample size. Homogeneous samples of 20 – 40 quasar lenses, with a combination of ancillary data (e.g. spectroscopy, time-delay monitoring, deep and high resolution imaging), would enable substantial progress on all fronts.

In order to assemble large samples of lensed quasars, wide areas of sky must be surveyed to overcome the intrinsic rarity of lenses. In the optical, this is made possible by ground-based surveys like the Sloan Digital Sky Survey (Abazajian et al. 2009), the Dark Energy Survey (hereafter DES, Sánchez & DES Collaboration 2010; Dark Energy Survey Collaboration et al. 2016), the VST-ATLAS (Shanks et al. 2015) and Pan-STARRS (Chambers et al. 2016). Various techniques have been developed to find quasar lenses, using morphological and spectroscopic information (as in the SQLS and BQLS, Oguri et al. 2006; Inada et al. 2012; More et al. 2016), image cutout modeling (Morgan et al. 2004; Schechter et al. 2017), data mining on catalog magnitudes (Agnello et al. 2015a; ?; Williams et al. 2017; Agnello 2017), variability (Berghea et al. 2017), and visual inspection of ‘blue-near-red’ objects (Lin et al. 2017; Diehl et al. 2017). In the radio, all-sky lens searches (such as CLASS and JVLA, Myers et al. 2003; King et al. 1999) examined radio-loud sources that could be resolved into multiple components by higher-resolution follow-up.

The search strategies depend on the quality of the data and on the specific kind of systems being sought. In fact, depending on the projected separation between multiple quasar images, and on the survey image quality and depth, quasar lenses may be catalogued as multiple sources with similar colours, or blended in one or more extended objects. The Gaia satellite mission (Gaia Collaboration et al. 2016; Lindegren et al. 2016; van Leeuwen et al. 2017), with sharp image quality (FWHM $\approx 0.2''$) and moderate depth ($G = 20.7$), can be combined with a near-infrared colour-based search from the WISE mission (Wright et al. 2010) to select quasar lenses as quasar-like objects that are resolved into multiple images. The method has been detailed elsewhere (Agnello 2017), here we illustrate its application to the DES year-3 footprint (Diehl et al. 2016).

In this paper, we report the discovery of two previously unknown lensed quasars, WGD2038-4008 (r.a.=20:38:02.65, dec.=−40:08:14.64) and WGD2021-4115 (r.a.=20:21:39.45, dec.=−41:15:57.11), from the joint use of WISE colour selection, Gaia multiplet detection, and DES image inspec-

tion. The same search, besides recovering known lenses, has yielded a list of potential doubles, as well as possible Galactic streams and substructure among the contaminants. Throughout this paper, we adopt the following nomenclature: *objects* denotes everything pre-selected via colour cuts; *targets* are objects that have been skimmed with additional techniques (a multiplet search, in this case); and *candidates* are targets that survive pixel-by-pixel examination, such as image cutout modeling or visual inspection. When a WISE source corresponds to multiple DES or Gaia detections, the one closest to the WISE position is denoted as *primary* and the remaining ones as *secondary*.

This paper is organized as follows. In Section 2 we describe our WISE-Gaia-DES search, the discovery of WGD2038-4008 and WGD2021-4115 and other candidates, and spectroscopic confirmation; multi-component fits to the cutouts and gravitational lens models in Section 3. In Section 4 we discuss the results and future prospects of this method. The paper is briefly summarized in Section 5. Following previous work, DES *grizY* magnitudes are given in the AB system and WISE magnitudes are in the Vega system.

2 THE WISE-GAIA-DES SEARCH, AND DISCOVERY OF LENSED QUASARS

Multiple data-mining techniques have been applied to the search of lensed quasars in the DES, over the last two years. Some objects were flagged independently within different searches (see tab. 1). WGD2038-4008 and WGD2021-4115 (shown in figures 1, 2) were discovered using a novel search combining WISE, Gaia and DES. General properties of this search strategy and numbers for other survey footprints are given by Agnello (2017), here we summarize the main steps: first, objects are first selected based on their WISE colours; then, those corresponding to multiple-source detections (i.e. ‘multiplets’) in Gaia are retained as targets; finally, DES image cutouts of targets are visually inspected to identify lens candidates. A variation on this theme will be illustrated in Section 4.1.

2.1 WISE-Gaia-DES search

The initial sample consisted of 173048 objects, selected in a footprint slightly larger than the DES-Y3 one, satisfying¹

$$W1 - W2 > 0.55, 2.2 < W2 - W3 < 3.8$$

$$W1 < 17.0, W2 < 15.4, W3 < 11.6,$$

$$\delta W1 < 0.25, \delta W2 < 0.3, \delta W3 < 0.35,$$

$$W2 - W3 < \max[2.7; 3.15 + 1.5(W1 - W2 - 1.075)] . \quad (1)$$

A cross-match with Gaia yielded 107076 sources, of which 2656 are unique multiplets - i.e. WISE sources corresponding to more than one non-duplicate Gaia detection within $6''$ from the corresponding WISE position. A significant subset of these (≈ 2000) lie within the DES-Y3 footprint.

¹ Here $W^{\prime}X^{\prime}$ and $\delta W^{\prime}X^{\prime}$ ($X^{\prime}=1,2,3$) refer to the magnitudes $w^{\prime}X^{\prime}_{\text{mpro}}$ and respective uncertainties $w^{\prime}X^{\prime}_{\text{sigmpro}}$ from the WISE catalogue.

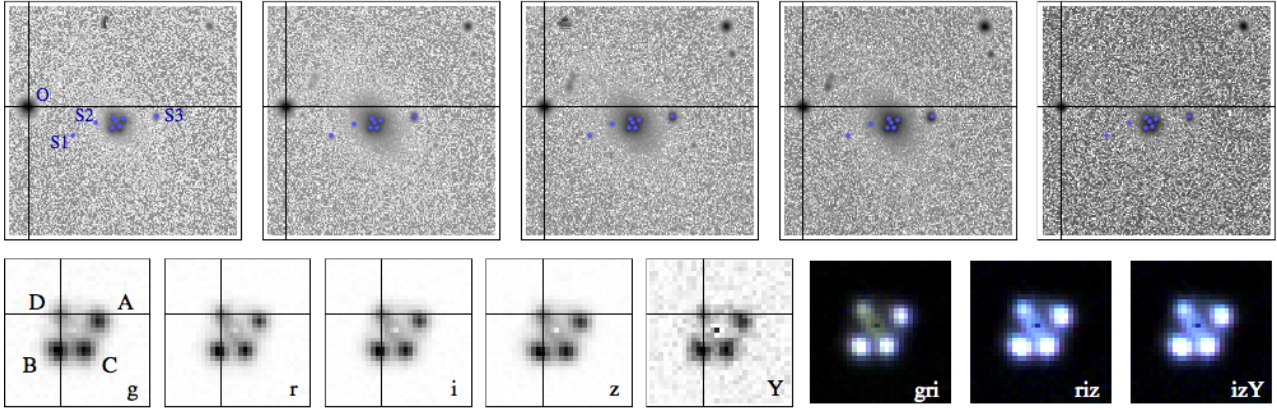


Figure 1. Single-epoch cutouts of WGD2038-4008. *Top:* $45.3'' \times 45.3''$ ($172\text{px} \times 172\text{px}$) *grizY* cutouts, showing the dominant ‘halo’ component of the deflector and a nearby bright star used to fit for the PSF; bullets mark the locations of the objects considered in the cutout modeling, including three sources marked as S1, S2, S3. *Bottom:* $7.9'' \times 7.9''$ ($30\text{px} \times 30\text{px}$) *grizY* cutouts and colour-composites, after subtracting the main ‘halo’ profile of the deflector; a flattened bulge, approximately as bright as the faintest quasar image, is visible in the *gri* cutouts. Images A, B, D, C are marked following the expected ordering in arrival times; the lens galaxy G is in the center.

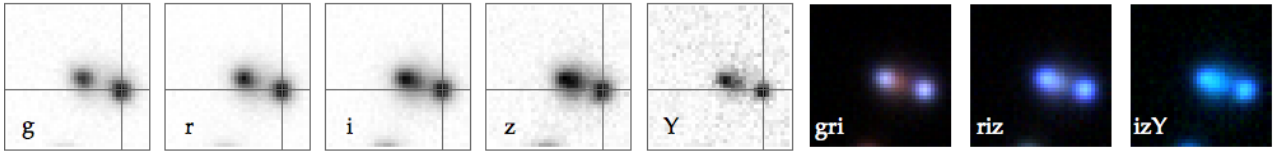


Figure 2. Single-epoch cutouts of WGD2021-4115: $7.9'' \times 7.9''$ ($30\text{px} \times 30\text{px}$) *grizY* cutouts and colour-composites. Axes intersect at image A (the farthest and with shortest arrival time); the counter-image B is blended with the lens G. Due to image quality and B-G proximity, uncertainties on astrometry and photometry in WGD2021-4115 are systematics-dominated.

This target list was narrowed down to a sample of 53 candidates by simple visual inspection of their DES images. Among these are some recently discovered lenses, which had been previously identified with other techniques (Aggello et al. 2015b; Lin et al. 2017, Anguita et al. in prep.). The WFI2033-4723 quad (Morgan et al. 2004) was identified as well, whereas WFI2026-4536 was excluded by the WISE colour pre-selection. In order to prioritize follow-up, candidates can be further graded based on how closely they resemble lenses, based mostly on two criteria: (i) the presence of two or more blue, compact sources with consistent colours across multiple bands; (ii) the presence of a (typically red) galaxy between the putative quasar images. Acceptable ‘new’ candidates identified within this search are shown in Figure 3 and listed in Table 1.

Some veritable multiplets may have been classified as duplicates in the Gaia-DR1, and so were not flagged by this search. A complementary search, using DES multiplets instead of Gaia-DR1, is outlined in Section 4.1. It recognized some WISE-Gaia multiplets, and gave at least two additional candidates (tab. 1) as WISE-DES multiplets that would correspond to WISE-Gaia singlets.

While other lens candidates would require spectroscopic follow-up for confirmation, WGD2038-4008 stood out due to its distinctive configuration, with four blue point-source images around a luminous red galaxy. Figure 1 shows multi-band wide-field cutouts of the system and a close-up, with our adopted naming convention for different components and nearby sources.

2.2 Spectroscopic confirmation

Both WGD2038-4008 and WGD2021-4115 were observed with long-slit spectroscopy, to secure their lens and source redshifts, as part of a campaign to obtain follow-up spectroscopy of the lens galaxy in various quasar lenses. To this aim, IMACS at the 6.5m Walter Baade Telescope at Magellan (Las Campanas) was used, set up in ‘long’ f/4 camera mode, covering the full $4000\text{\AA} - 12000\text{\AA}$ wavelength range. For WGD 2038-4008, the slit was simply oriented North-South and centered on the lens galaxy; since WGD2021-4115 required proper spectroscopic confirmation, the slit was oriented along the two blue images.

Figure 4 shows the extracted spectra of both systems. From emission lines, the source redshifts of the quad and double are $z_s = 0.777 \pm 0.001$ and $z_s = 1.390 \pm 0.001$, respectively. Absorption features, compatible with $z_l = 0.230 \pm 0.002$ on the quad and $z_l = 0.335 \pm 0.002$ on the double, are also identified.

3 CUTOUT MODELS AND LENS PROPERTIES

Simple lens properties can be obtained by modeling the DES image cutouts. In particular, from the *grizY* survey images we obtained photometry and relative astrometry of multiple components in the two confirmed lenses, and simple lens models based on those.

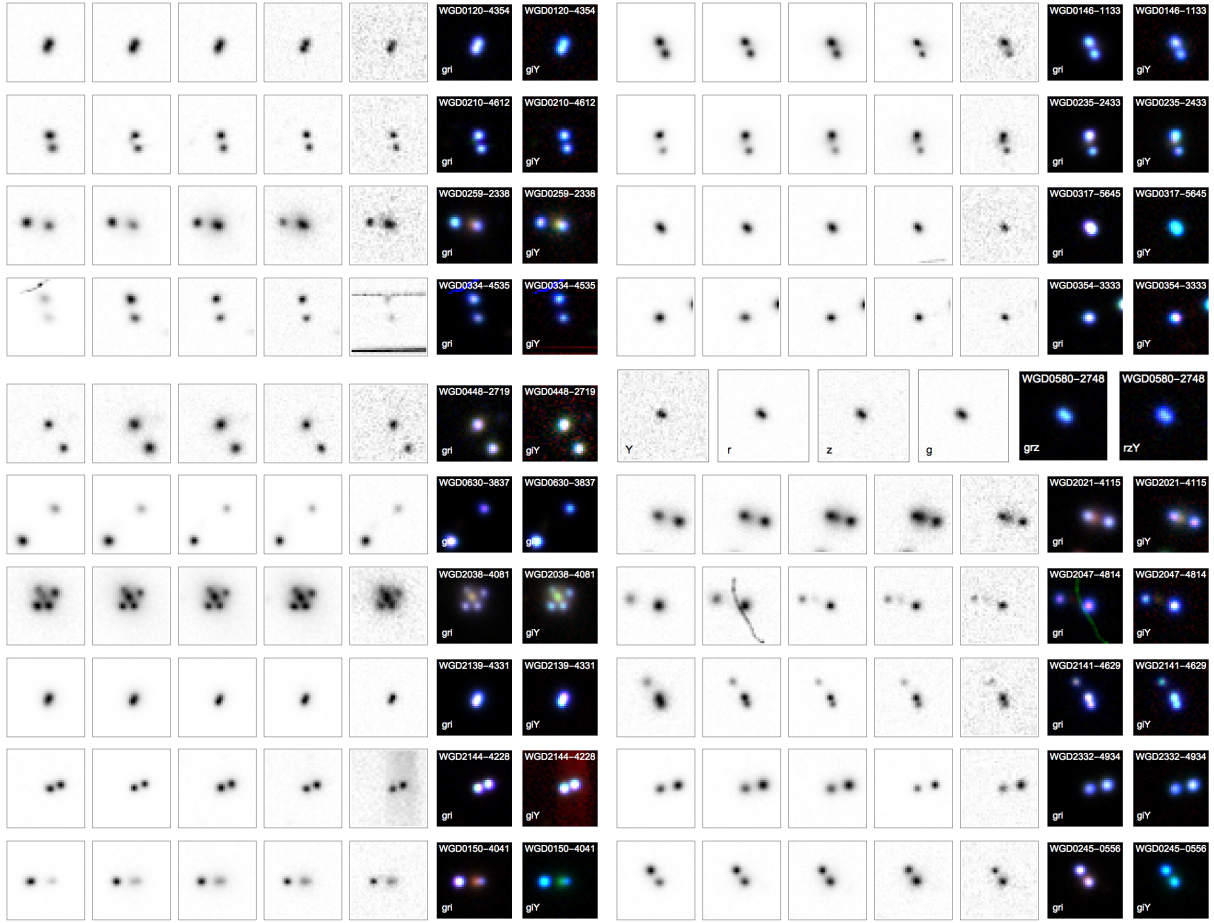


Figure 3. DES single-epoch cutouts of high-grade, multiplet-selected candidates that are not already known lenses. The last two (WGD0150-4041, WGD0245-0556) have been found among DES multiplets, and correspond to singlets in Gaia-DR1. Three multiplets (WGD0259-2338, WGD0146-1133, WGD0235-2433) have also been identified as WISE-Gaia multiplets in the ATLAS-DR3 footprint, where they have coverage in just two bands.

3.1 WGD2038-4008: system configuration and gravitational lens models

WGD2038-4008 has a quite symmetric configuration: two saddle-point images aligned along the major axis of the deflector, and the two minima on a nearly perpendicular line. These components are all blended together by the DES pipeline, but can be disentangled by modeling the DES cutouts as a superposition of four point-sources and a galaxy, for which we choose a single Sérsic profile (Sérsic 1968).

3.1.1 Photometry and Astrometry of WGD2038-4008

We use a nearby, bright point source (indicated as ‘O’ in fig. 1) to directly model the point-spread function (PSF) and the slight offset among different bands. In each band, the PSF is well fit (to within 10%) by a superposition of three concentric Gaussians with the same axis ratios and orientations, contributing 61%, 33% and 6% of the total flux in the core, wings and outskirts respectively. Residuals from PSF mismatch are due to multipolar features that are not captured by these simple models.

Table 2 lists the relative positions and *grizY* magnitudes of the four images (A,B,C,D), deflector (G) and three

additional sources (S1, S2, S3). The deflector has a compact bulge and an extended and luminous ‘halo’, which contributes most of the light and is fit by a Sérsic profile with $R_{\text{eff}} = (3.45 \pm 0.12)''$, $n_s = 1.90 \pm 0.05$, axis ratio $q = 0.77 \pm 0.01$ and p.a. $\phi_l = (41.6 \pm 1.6) \text{ deg}$ (E of N). Faint features in blue bands are visible, with isophotes twisting towards 30deg East of North. Contamination by the deflector affects the position and fluxes of image D, whose uncertainties are systematics-dominated.

3.1.2 Properties of the deflector galaxy

From the magnitudes of G as measured from the cutouts, we can infer its stellar mass. To this aim, we use the FAST code (Kriek et al. 2009), with an exponentially-declining star-formation history and a Salpeter stellar IMF. We adopt the nominal magnitude uncertainties ($\delta m = 0.016$) from Table 2, obtaining $\log_{10}(M_*/M_\odot) = 11.40^{+0.01}_{-0.08}$. The highly skewed confidence intervals for M_* , are a consequence of the small (statistical) uncertainties on the measured magnitudes and, consequently, of the steepness of the 4000\AA break. With current, broad-band data, different stellar templates are indistinguishable.

Simple lens models can be fit using the measured im-

name	r.a.	dec.	i (mag)
WGD0120-4354 ^(d)	20.026573	-43.911281	19.09
WGD0146-1133 ^(a,d)	26.636987	-11.560821	17.48
WGD0210-4612	32.728207	-46.214376	19.49
WGD0235-2433 ^(a)	38.864257	-24.553678	17.12
WGD0259-2338 ^(a)	44.889649	-23.63383	18.41
WGD0317-5645 ^(d)	49.429068	-56.081904	18.74
WGD0334-4535	53.672139	-45.064588	19.90
WGD0354-3333	58.738739	-33.560711	19.04
WGD0448-2719	72.180042	-27.325524	19.22
WGD0508-2748	77.013318	-27.80528	19.23
WGD0630-3837	90.783347	-38.628656	18.64
WGD2021-4115	305.414396	-41.265865	18.51
WGD2038-4008	309.511278	-40.137107	16.50
WGD2047-4814 ^(c,d)	311.862059	-48.029964	19.11
WGD2139-4331	324.988092	-43.517187	17.58
WGD2141-4629 ^(d)	325.453535	-46.496119	18.95
WGD2144-4228	316.18399	-42.481507	17.73
WGD2332-4934	353.042968	-49.568522	18.98
WGD0150-4041 ^(b)	27.736921	-40.695568	18.66
WGD0245-0556 ^(b)	41.356506	-5.950145	18.73

Table 1. Concise list of high-grade, multiplet-selected lens candidates that are not already known lenses. The i -band (`wavg_mag_auto`) magnitude refers to the primary DES match of each WISE-detected object, which is often a blend of multiple components. ^(a) The same search over the ATLAS-DR3 footprint has yielded candidates that also lie in the DES footprint. ^(b) The last two candidates have been identified among DES multiplets that correspond to Gaia singlets. ^(c) Long-slit spectroscopy (SOAR-Goodman, PI V. Motta) excludes WGD2047-48 as a line-of-sight alignment of a narrow-line-galaxy at $z = 0.33$ with a red galaxy and a blue star. ^(d) Some of the WISE-Gaia candidates had also been identified independently, with other techniques, in the STRIDES-2016 campaign (Anguita et al., Treu et al.; in prep.).

age positions as constraints. We do not consider flux-ratio constraints, as they can be easily affected by differential reddening, microlensing and time-delays (e.g. Yonehara et al. 1999). We adopt a singular isothermal ellipsoid for the deflector, with deflections

$$\alpha_X = -\frac{b}{\sqrt{1-q^2}} \arctan\left(\frac{X\sqrt{1-q^2}}{\sqrt{q^2X^2+Y^2}}\right) \quad (2)$$

$$\alpha_Y = -\frac{b}{\sqrt{1-q^2}} \operatorname{arctanh}\left(\frac{Y\sqrt{1-q^2}}{\sqrt{q^2X^2+Y^2}}\right) \quad (3)$$

in a system aligned along the principal axes (X, Y) of G. Here, the deflector is described solely by its lens strength b and axis ratio q , besides its position angle ϕ_l . We add an external shear component with uniform prior on the amplitude within $0.0 < \gamma_s < 0.14$ and uniform prior of the shear angle $0.0 < \phi_s < \pi$, and explore three different choices for the deflector shape parameters: (a) priors on q and ϕ_l centered on those from cutout modeling, with larger adopted uncertainties of 0.1 and 10 deg respectively; (b) ϕ_l fixed to its value from cutout models, and q free to vary; (c) uniform priors on q, ϕ_l . In all models, the Einstein radius $\theta_E = b/\sqrt{q}$ has a uniform prior between $1.0''$ and $3.0''$.

Table 3 shows the lens model results. The Einstein radius is quite robust against the adopted priors, and approximately half the A-B image separation. The lens position angle is always close to those observed from the cutouts,

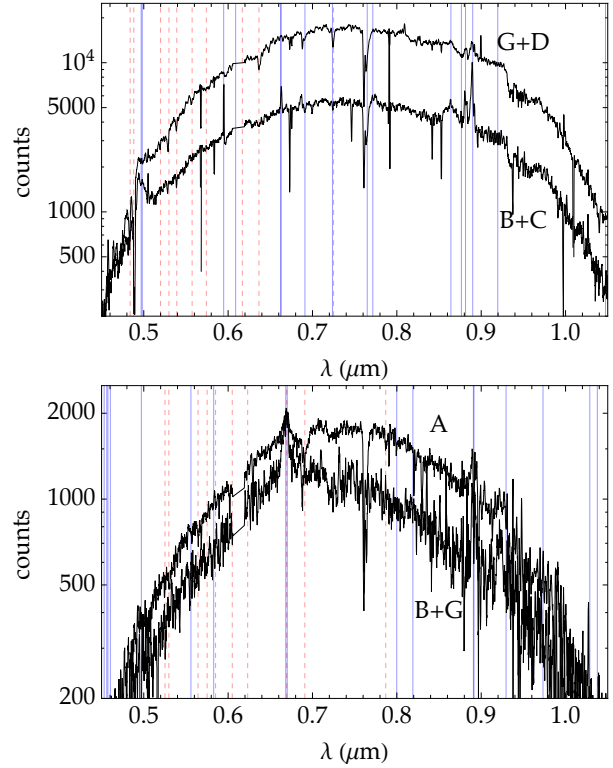


Figure 4. Long-slit spectra of WGD2038-4008 (*top*) and WGD2021-4115 (*bottom*) from Magellan-IMACS follow-up.

whereas a significant shear-ellipticity degeneracy is present. More accurate lens models should account for the variation in shape and position angle of the observed isophotes (e.g. by using a superposition of ellipsoidal models), and possibly incorporate observations of galaxies in the vicinity of the lens in projection, to independently assess the shear component.

3.2 WGD2021-4115: system configuration and gravitational lens models

WGD2021-4115 consists of two quasar images at either side of a round, faint, red galaxy (fig. 2). We denote the farther image (with shorter arrival time) as A. Its counterimage B lies very close to the deflector galaxy. The same approach as above has been followed for WGD2021-4115, obtaining object positions and $grizY$ magnitudes from the DES image cutouts and performing simple lens models. The astrometry and photometry of the three components is given in Table 2. In this case, G is smaller, fainter, and very close to image B, which makes the cutout models highly degenerate. The structural parameters of G cannot be recovered reliably, and its magnitudes have significant uncertainties.

From simple lens models, a high quadrupole component (shear $\gamma_s = 0.20 \pm 0.04$ or flattening $q = 0.50 \pm 0.08$) is needed to account for the off-centering of images A, B with respect to the lens galaxy, still producing only two quasar images due to the highly asymmetric configuration. The Einstein radius ($(1.25 \pm 0.05)''$ from SIE, $(1.06 \pm 0.07)''$ from SIS+XS) is comparable to half the A-B image separation, but due to the significant quadrupole it depends appreciably on the chosen lens model.

obj.	comp.	$\delta x''$ = $-\delta r.a. \cos(\text{dec.})$	$\delta y''$ $\delta \text{dec.}$	g	r	i	z	Y
J2038-4008	A	0.00±0.04	0.0±0.04	20.22±0.03	19.74±0.03	19.24±0.03	18.67±0.03	18.96±0.03
	B	-2.22 ± 0.05	-1.59 ± 0.05	20.08±0.04	19.45±0.04	18.98±0.04	18.50±0.05	18.71±0.03
	C	-0.79 ± 0.05	-1.54 ± 0.06	20.17±0.04	19.50±0.04	19.08±0.03	18.58±0.03	18.66±0.03
	D	-2.01 ± 0.05	0.27 ± 0.07	20.99±0.05	19.91±0.06	19.42±0.06	19.95±0.05	19.24±0.10
	G	-1.38 ± 0.04	-0.45 ± 0.06	19.18±0.015	18.02±0.016	17.54±0.016	17.19±0.016	16.80±0.015
	S1	-9.96 ± 0.06	-3.17 ± 0.07	24.10±0.03	22.48±0.03	22.12±0.02	21.87±0.03	21.82±0.07
	S2	-5.57 ± 0.15	-0.71 ± 0.09	[27.5 ± 0.6]	[25.1 ± 0.5]	22.82±0.08	21.93±0.08	21.33±0.08
	S3	6.58 ± 0.06	0.68 ± 0.04	21.82±0.01	20.57±0.03	19.21±0.02	18.79±0.03	18.49±0.02
J2021-4115	A	0.00±0.06	0.0±0.06	19.81±0.01	18.90±0.01	18.73±0.01	18.53±0.02	18.29±0.01
	B	-2.50±0.13	0.75±0.13	19.80±0.03	18.80±0.07	18.86±0.10	18.60±0.10	18.53±0.07
	G	-2.04±0.13	0.46±0.13	—	—	20.2±0.4	19.9±0.3	19.5±0.3

Table 2. Positions (relative to image A) and magnitudes of the objects in the two lenses, from a joint model of the DES *grizY* single-epoch images with best image quality. The quasar images are named according to the expected time-delays. *Top*: photometry and (relative) astrometry of WGD2038-4008. The PSF is fit directly to the bright star in fig. 1, and three nearby compact sources are included in the fit, in order to limit systematic uncertainties on positions and magnitudes. The magnitudes quoted for G are from the main halo component, whose light dominates over the compact bulge (visible in the residuals), which is roughly as bright as image D. Uncertainties on displacements and magnitudes of image D are systematically dominated, due to contamination by G. Magnitudes in square brackets (for source S2) may be significantly affected by noise and contamination by G. *Bottom*: photometry and (relative) astrometry of WGD2021-4115. The PSF is fit to the farthest image A, together with positions and magnitudes of the three components. The cutout image quality, proximity of B and G, and small extent of G render the fitted positions and magnitude significantly uncertain.

obj.	mod.	θ_E ('')	q	ϕ_l (deg. E of N)	ϕ_s (deg. N of W)	γ_s	δx_G ('')	δy_G ('')
J2038-4008	mod.(a)	1.26±0.03	0.79±0.05	42.0±7.7	25.0±7.0	0.095±0.025	-0.04±0.03	0.04±0.04
	mod.(b)	1.26±0.05	0.64 ± 0.22	42.0 ± 7.0	18.0±35.0	0.07 ± 0.04	-0.06±0.04	0.05±0.04
	mod.(c)	1.32±0.04	0.44±0.06	32.2±5.05	-75.4 ± 50.3	0.02 ± 0.02	-0.06 ± 0.04	0.05 ± 0.04
J2021-4115	mod.(a)	1.25±0.05	0.50±0.08	8.0±4.0	—	[0.0]	0.02±0.06	0.00±0.06
	mod.(b)	1.06±0.07	[1.0]	—	-11.0±5.0	0.21±0.04	0.03±0.06	0.02±0.06

Table 3. Lens model parameters: Einstein radius $\theta_E = b/\sqrt{q}$, axis ratio q , and p.a. ϕ_l of the main lens; external shear angle ϕ_s and amplitude γ_s ; and lens center $(\delta x_G, \delta y_G)$ with respect to the galaxy center identified in the DES cutouts. Image positions are fit with a SIE for the deflector (G) and external shear to account for possible external contributions. Different lines correspond to different priors adopted on the shape parameters q, ϕ_l of G (see text).

4 DISCUSSION

The combination of WISE colour selection and Gaia/DES image quality and depth has resulted in the discovery of the lensed quasar quad WGD2038-4008 and a sample of high-grade candidate doubles, among which WGD2021-4115 was spectroscopically followed up and confirmed. Due to different survey strategy, source-detection pipelines, and depth and image quality, Gaia can detect multiple sources that are unrecognized in DES and *vice versa*. Also, the current performance of the WISE-Gaia multiplet search is limited by the pre-selection cuts in WISE and absence of colour information in Gaia-DR1. These aspects are discussed below.

4.1 DES multiplets

The WISE-Gaia search took 173048 input positions, but resulted in fewer (107076) output detections. This is mostly because of the current Gaia-DR1 completeness towards faint magnitudes, and pipeline-specific choices in source detection and deblending. By contrast, a WISE-DES match resulted in 206671 entries, meaning that $\approx 50 \times 10^3$ WISE objects correspond to multiple DES-detected sources within a search

radius of $10''$. This suggests that some interesting objects are missed or mis-classified by Gaia but can be recovered within DES multiplets.

On the other hand, many WISE-DES multiplets can contain very faint objects, mostly galaxies, or line-of-sight alignments of extragalactic objects with foreground stars. Foreground star contamination is already present in the WISE-Gaia selection, as the distribution of multiplets is more abundant towards the Galactic disc, the Large Magellanic Cloud and along four candidate streams (designated as WG1,...,WG4 by Agnello 2017). In a WISE-DES multiplet search, *grizY* magnitudes can be used to infer which multiplets are most likely contaminants, and which ones are more promising, as one can expect a qso+star alignment to show two well-separated objects, possibly with different colours.

A simple search can then exclude multiplets with separation $\gtrsim 3''$ and with at least one point-source, or multiplets whose primary has promising quasar colours ($g - i < 0.85$) and a colour difference $|\delta(g - i)| > 0.4$ between primary and secondary detected sources. The separation criterion is chosen because, at large Einstein radii, the lens galaxy should be detectable by the DES pipeline.

If this selection is effective, what remains should be al-

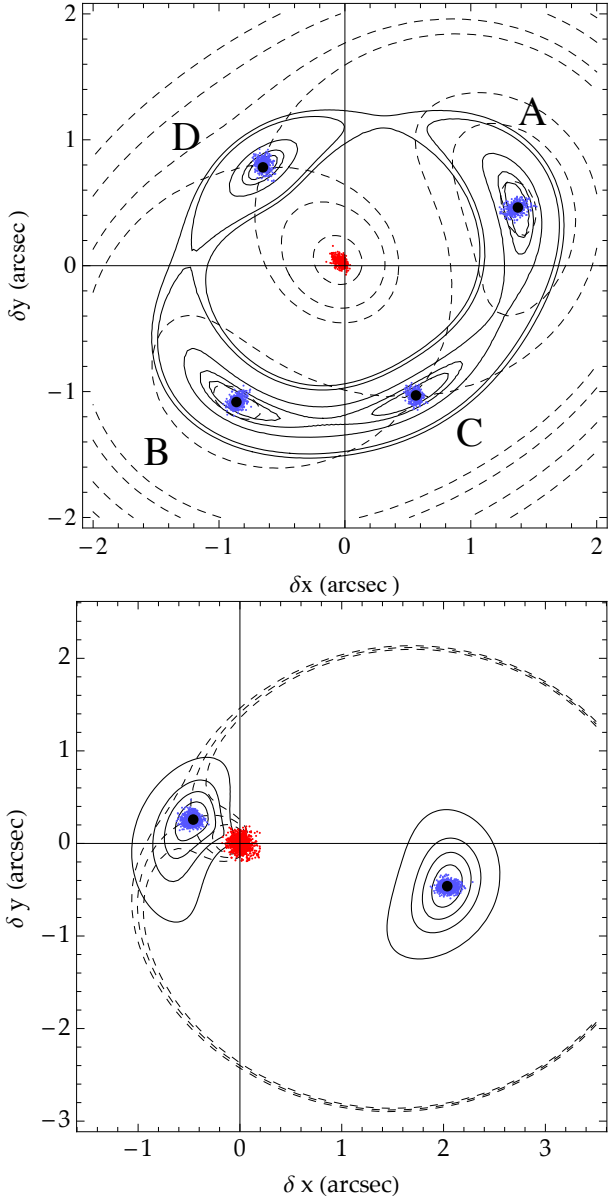


Figure 5. Lens properties from cutout modeling: best-fit SIE models (see tab. 3), with arrival-time contours (dashed) and images of circular source-plane isophotes (full lines), for WGD2038-4008 (*top*) and WGD2021-4115 (*bottom*).

most uniformly distributed over the DES footprint. For a first assessment of the efficiency of this procedure, and account for footprint coverage, one can simply plot the distribution of different systems. Figure 6 shows the distribution of WISE-DES singlets, WISE-DES multiplets that survive the above cuts in separation and colour difference, and WISE-DES multiplets that should be mostly extragalactic+star alignments. Three distributions are shown, corresponding to singlets/multiplets whose primary has $23.0 > i > 21.75$, $21.75 > i > 20.5$, and $20.5 > i$ respectively. The magnitude separation is used to understand whether contamination is more significant towards faint objects, or in specific regions of the sky – e.g. by the thick-stream candidates WG1,...,WG4 (Agnello 2017, also Shipp et al. in prep.) mentioned above.

The fourth column displays their distribution regardless of primary magnitude. The blue points in the last row show the distribution of all WISE-Gaia multiplet targets from Section 2. Among the WISE-DES multiplets with acceptable configurations and colour differences, many have extended morphology², a secondary with $g - i > 1$, and small colour differences ($|\delta(g - i)| < 0.2$, $|\delta(r - z)| < 0.2$). They can be interpreted as pairs of compact narrow-line galaxies, a common contaminant in quasar lens searches without u -band information. A naïve selection may then require $g - i < 0.85$ for all sources. The resulting multiplets with primary $i < 20.5$ are shown by blue dots in the second row of Figure 6, and amount to 233 (resp. 179, 405) pairs with secondary $i < 20.5$ (resp. $20.5 < i < 21.75$, $21.75 < i < 23.0$). These have been visually inspected, finding some WISE-Gaia candidates independently and yielding at least two good candidates that corresponded to Gaia-DR1 singlets (see tab. 1, fig. 3).

4.2 Future prospects

This search has mostly relied on a WISE-Gaia preselection, with a final step of DES image inspection. The WISE colour pre-selection, tailored on the majority of known lenses, may nonetheless be too restrictive, as it discards some known lenses (including quads) in the remaining ‘upper wedge’ $W2 - W3 > 3.15 + 1.5(W1 - W2 - 1.075)$. A crude estimate, based on the number of known lenses that lie in the excluded region, suggests that a further $\approx 50\%$ of targets (and possibly candidates) can be identified there.

While quads like WGD2038-4008 need little follow-up for confirmation, spatially-resolved spectroscopy of candidate doubles is necessary. A clear example is given by WGD2047-4814 (tab. 1, fig. 3): it had already been selected with a different technique (Agnello et al. 2015a) in DES-Y2 and prioritized as a high-grade candidate, but it was recognized by long-slit spectroscopy (SOAR-Goodman, PI V. Motta) as a $z = 0.33$ narrow-line galaxy aligned with a red galaxy and a blue star (Motta, 2017, private communication). In order to facilitate follow-up, we list the coordinates and i -band magnitudes of some high-rank candidates.

A key component of this investigation was the detection of Gaia multiplets, not flagged as duplicate detections, within a $6''$ search radius from WISE-selected quasars. Given the Gaia scanning strategy and object-detection pipeline, some actual multiplets may have been flagged as duplicates in the Gaia-DR1 catalogue. In fact, only about 20–30% of known lenses are currently recognized as multiple unique sources in Gaia-DR1. Future releases may alleviate this issue, since each object is visited multiple times and with different orientations. A complementary search, examining WISE-DES multiplets, may refine the distance/colour cuts explored above (Sect. 4.1), adopting a population-mixture approach for pairs/multiplets of objects. This may, in fact, be possible already at the level of Gaia colours, as Gaia-DR2 is also providing ‘blue’ and ‘red’ internal magnitudes.

² The DES pipeline assigns every detected object a probability of being an extended source.

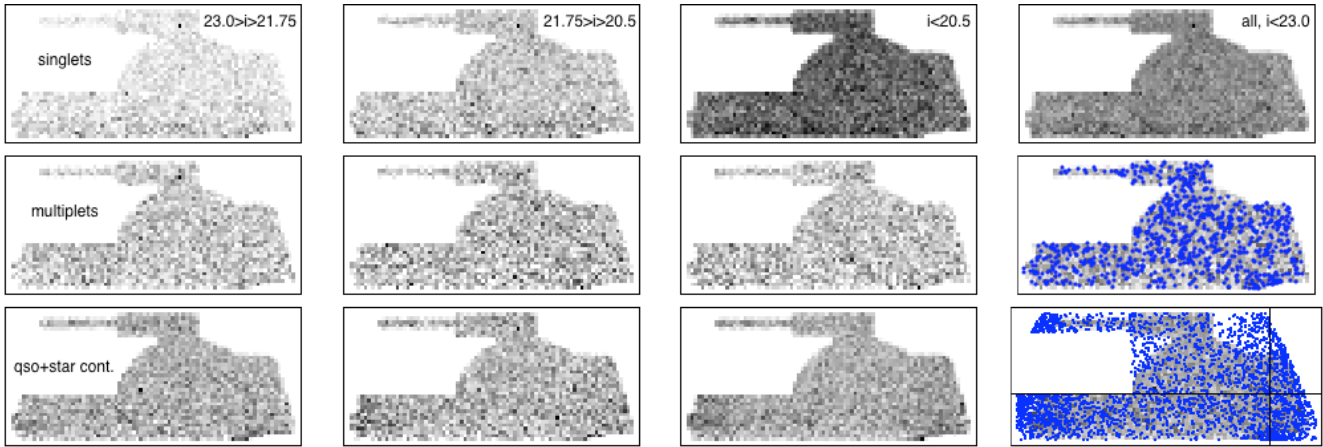


Figure 6. WISE-DES singlets and multiplets. Each row of density maps corresponds to a different macro-class: WISE sources corresponding to DES singlets; WISE sources corresponding to (possibly) extragalactic multiplets; and WISE sources corresponding to multiplets that likely contain a foreground star. In the second line, blue points mark WISE-DES multiplets whose primary has $i < 20.5$ (`wav_mag_auto`); in the third line, the blue points are the 2656 WISE-Gaia target multiplets. The candidate streams WG1,...,WG4 of Agnello (2017) can be mapped in different magnitude slices; axes intercept at the location of the Globular Cluster NGC 1851.

5 SUMMARY

We have presented the first results of a new search for lensed quasars based on the combination of mid-infrared photometry from WISE, high resolution images from Gaia, and multiband optical imaging from DES. This search has found already-known lenses and some new ones discovered during the STRIDES-2016 campaigns³, and it yielded ≈ 50 quasar lens candidates in the DES-Y3 footprint, of which 18 high-grade candidates are presented in this paper (tab. 1, fig.3).

Out of these, WGD2038-4008 is a quadruply lensed quasar, not previously found with other techniques. Its deflector is a massive ($\log(M_*/M_\odot) \approx 11.5$) and low-redshift ($z_l \approx 0.23$) luminous red galaxy, with a compact bulge, a bright halo contributing most of the light, and indication of isophotal shape variations at large distances. Simple lens models can be well fit to its image configuration. The deflector shape parameters obtained from lensing are in general agreement with those observed from the DES *grizY* cutouts, but there are significant quadrupole degeneracies that will need follow-up imaging to be resolved. The Einstein radius is quite robustly constrained at $(1.30 \pm 0.04)''$, whereas the main ‘halo’ component of the deflector has half-light radius $R_{\text{eff}} = (3.45 \pm 0.12)''$.

The double WGD2021-4115 has been followed up spectroscopically and confirmed as a lens. Its configuration has an arrival-time minimum (image A) well separated from the blend of arrival-time saddle-point (image B) and deflector. A high quadrupole component is expected from our first lens models, and the Einstein radius ($1.3'' > \theta_E > 1.0''$) can vary appreciably because of this.

The WISE-Gaia-DES multiplet search can be further developed in multiple ways. Multi-band information from DES can be used to augment the multiplet detection, by pruning different classes of contaminants. The WISE colour pre-selection can be performed with looser cuts, or within a

population-mixture classification to exclude the most abundant contaminant classes. Furthermore, chromatic information will be available since Gaia-DR2 (due apr.1st 2018), and spectra of most Gaia detections will be available upon completion (2020). In fact, WGD2038-4008 already has a (spatially unresolved) spectrum in the 6dFGS, where the image quality of older imaging surveys precluded its identification as a lensed quasar.

With this work, we have demonstrated the effectiveness of the WISE-Gaia lens search, discovering new lenses (among which a quadruple), that could not be found with previously developed techniques. At this stage, however, the quantification of how different search techniques are complementary is premature, as comprehensive samples with spectroscopic follow-up are needed to that purpose. Our results suggest that a significant population of lensed quasars may still be found in current surveys, enabling the collection of lens samples for studies of distant quasars (both their hosts and central engines), luminous and dark matter in galaxies over a range of redshifts, and cosmography.

ACKNOWLEDGMENTS

This paper was written as part of the STRong lensing Insights into the Dark Energy Survey (STRIDES) collaboration, a broad external collaboration of the Dark Energy Survey, <http://strides.astro.ucla.edu>

TT acknowledges support from NSF through grant AST-1450141, and from the Packard Foundation through a Packard Research Fellowship. CDF acknowledges support from the US National Science Foundation through grant number AST-1312329.

Funding for the DES Projects has been provided by the DOE and NSF(USA), MISE(Spain), STFC(UK), HEFCE(UK). NCSA(UIUC), KICP(U. Chicago), CCAPP(Ohio State), MIFPA(Texas A&M), CNPQ, FAPERJ, FINEP (Brazil), MINECO(Spain), DFG(Germany) and the Collaborating Institutions in the Dark Energy Survey. The Collaborating Institutions are

³ Treu et al., and accompanying discovery papers, currently in prep.

Argonne Lab, UC Santa Cruz, University of Cambridge, CIEMAT-Madrid, University of Chicago, University College London, DES-Brazil Consortium, University of Edinburgh, ETH Zürich, Fermilab, University of Illinois, ICE (IEEC-CSIC), IFAE Barcelona, Lawrence Berkeley Lab, LMU München and the associated Excellence Cluster Universe, University of Michigan, NOAO, University of Nottingham, Ohio State University, University of Pennsylvania, University of Portsmouth, SLAC National Lab, Stanford University, University of Sussex, and Texas A&M University. The DES Data Management System is supported by the NSF under Grant Number AST-1138766. The DES participants from Spanish institutions are partially supported by MINECO under grants AYA2012-39559, ESP2013-48274, FPA2013-47986, and Centro de Excelencia Severo Ochoa SEV-2012-0234. Research leading to these results has received funding from the ERC under the EU's 7th Framework Programme including grants ERC 240672, 291329 and 306478.

This research has made use of the NASA/ IPAC Infrared Science Archive, which is operated by the Jet Propulsion Laboratory, California Institute of Technology, under contract with the National Aeronautics and Space Administration.

This work has made use of data from the European Space Agency (ESA) mission Gaia (<https://www.cosmos.esa.int/gaia>), processed by the Gaia Data Processing and Analysis Consortium (DPAC), <https://www.cosmos.esa.int/web/gaia/dpac/consortium>. Funding for the DPAC has been provided by national institutions, in particular the institutions participating in the Gaia Multilateral Agreement.

This work is based in part on observations obtained at the Southern Astrophysical Research (SOAR) telescope, which is a joint project of the Ministério da Ciência, Tecnologia, e Inovação (MCTI) da República Federativa do Brasil, the U.S. National Optical Astronomy Observatory (NOAO), the University of North Carolina at Chapel Hill (UNC), and Michigan State University (MSU).

AA wishes to thank the ITC-Harvard for hospitality in February and June 2017, when most of the work reported here was made.

REFERENCES

- Abazajian, K. N., Adelman-McCarthy, J. K., Agüeros, M. A., et al. 2009, *ApJS*, 182, 543
- Agnello, A., Kelly, B. C., Treu, T., & Marshall, P. J. 2015, *MNRAS*, 448, 1446
- Agnello, A., Treu, T., Ostrovski, F., et al. 2015, *MNRAS*, 454, 1260
- Agnello, A. 2017, *MNRAS* in press, arXiv:1705.08900
- Anguita, T., Faure, C., Yonehara, A., et al. 2008, *AA*, 481, 615
- Bate, N. F., Floyd, D. J. E., Webster, R. L., & Wyithe, J. S. B. 2011, *ApJ*, 731, 71
- Berghea, C. T., et al., arXiv:1705.08359
- Chambers, K. C., Magnier, E. A., Metcalfe, N., et al. 2016, arXiv:1612.05560
- Dalal, N., & Kochanek, C. S. 2002, *ApJ*, 572, 25
- Dark Energy Survey Collaboration, Abbott, T., Abdalla, F. B., et al. 2016, *MNRAS*, 460, 1270
- Diehl, H. T., Neilsen, E., Gruendl, R., et al. 2016, *Proc. SPIE*, 9910, 99101D
- Diehl, H. T., Buckley-Geer, E., Lindgren, K., et al. 2017, *ApJS*, 232, 15
- Ding, X., Liao, K., Treu, T., et al. 2017, *MNRAS*, 465, 4634
- Gaia Collaboration, Prusti, T., de Bruijne, J. H. J., et al. 2016, *AA*, 595, A1
- Gilman, D., Agnello, A., Treu, T., Keeton, C. R., & Nierenberg, A. M. 2017, *MNRAS*, 467, 3970
- Jones, D. H., Saunders, W., Colless, M., et al. 2004, *MNRAS*, 355, 747
- Jones, D. H., Read, M. A., Saunders, W., et al. 2009, *MNRAS*, 399, 683
- Hutsemékers, D., Sluse, D., Braibant, L., & Anguita, T. 2015, *AA*, 584, A61
- Hsueh, J.-W., Oldham, L., Spingola, C., et al. 2017, *MNRAS*, 469, 3713
- Inada, N., Oguri, M., Shin, M.-S., et al. 2012, *AJ*, 143, 119
- King, L. J., Browne, I. W. A., Marlow, D. R., Patnaik, A. R., & Wilkinson, P. N. 1999, *MNRAS*, 307, 225
- Kriek, M., van Dokkum, P. G., Labbé, I., et al. 2009, *ApJ*, 700, 221
- van Leeuwen, F., Evans, D. W., De Angeli, F., et al. 2017, *AA*, 599, A32
- Lin, H., Buckley-Geer, E., Agnello, A., et al. 2017, *ApJL*, 838, L15
- Lindgren, L., Lammers, U., Bastian, U., et al. 2016, *AA*, 595, A4
- Mao, S., & Schneider, P. 1998, *MNRAS*, 295, 587
- More, A., Oguri, M., Kayo, I., et al. 2016, *MNRAS*, 456, 1595
- Morgan, N. D., Caldwell, J. A. R., Schechter, P. L., et al. 2004, *AJ*, 127, 2617
- Motta, V., Mediavilla, E., Rojas, K., et al. 2017, *ApJ*, 835, 132
- Myers, S. T., Jackson, N. J., Browne, I. W. A., et al. 2003, *MNRAS*, 341, 1
- Oguri, M., Inada, N., Pindor, B., et al. 2006, *AJ*, 132, 999
- Oguri, M., Rusu, C. E., & Falco, E. E. 2014, *MNRAS*, 439, 2494
- Peng, C. Y., Impey, C. D., Rix, H.-W., et al. 2006, *ApJ*, 649, 616
- Rahman, M., Ménard, B., Scranton, R., Schmidt, S. J., & Morrison, C. B. 2015, *MNRAS*, 447, 3500
- Rahman, M., Mendez, A. J., Ménard, B., et al. 2016, *MNRAS*, 460, 163
- Refsdal, S. 1964, *MNRAS*, 128, 307
- Sánchez, E., & DES Collaboration 2010, *Journal of Physics Conference Series*, 259, 012080
- Schechter, P. L., Pooley, D., Blackburne, J. A., & Wambsganss, J. 2014, *ApJ*, 793, 96
- Schechter, P. L., Morgan, N. D., Chehade, B., et al. 2017, *AJ*, 153, 219
- Sersic, J. L. 1968, *Cordoba, Argentina: Observatorio Astronomico*, 1968,
- Shanks, T., Metcalfe, N., Chehade, B., et al. 2015, *MNRAS*, 451, 4238
- Sluse, D., Hutsemékers, D., Courbin, F., Meylan, G., & Wambsganss, J. 2012, *AA*, 544, A62
- Suyu, S. H., Bonvin, V., Courbin, F., et al. 2017, *MNRAS*,

468, 2590
 Williams, P., Agnello, A., & Treu, T. 2017, MNRAS, 466, 3088
 Wright, E. L., Eisenhardt, P. R. M., Mainzer, A. K., et al. 2010, AJ, 140, 1868-1881
 Yonehara, A., Mineshige, S., Fukue, J., Umemura, M., & Turner, E. L. 1999, AA, 343, 41

AFFILIATIONS

¹European Southern Observatory, Karl-Schwarzschild-Strasse 2, 85748 Garching bei München, DE
²Fermi National Accelerator Laboratory, Batavia, IL 60510
³Departamento de Ciencias Físicas, Universidad Andres Bello Fernandez Concha 700, Las Condes, Santiago, Chile
⁴MIT Kavli Institute for Astrophysics and Space Research, 37-664G, 77 Massachusetts Avenue, Cambridge, MA 02139
⁵Department of Physics and Astronomy, PAB, 430 Portola Plaza, Box 951547, Los Angeles, CA 90095-1547, USA
⁶Instituto de Física y Astronomía, Universidad de Valparaíso, Avda. Gran Bretaña 1111, Playa Ancha, Valparaíso 2360102, Chile
⁷Institute for Astronomy, Department of Physics, ETH Zurich, Wolfgang-Pauli-Strasse 27, 8093, Zurich, Switzerland
⁸Institute of Astronomy, Madingley Road, Cambridge CB3 0HA, UK
⁹Laboratoire d'Astrophysique, Ecole Polytechnique Fédérale de Lausanne (EPFL), Observatoire de Sauvigny, CH-1290 Versoix, Switzerland
¹⁰Department of Physics, University of California Davis, 1 Shields Avenue, Davis, CA 95616, USA
¹¹Kavli IPMU (WPI), UTIAS, The University of Tokyo, Kashiwa, Chiba 277-8583, Japan
¹²Kavli Institute for Particle Astrophysics and Cosmology, Stanford University, 452 Lomita Mall, Stanford, CA 94305, USA
¹³Kavli Institute for Cosmology, University of Cambridge, Madingley Road, Cambridge CB3 0HA, UK
¹⁴Max-Planck-Institut für Astrophysik, Karl-Schwarzschild-Str. 1, D-85741 Garching, Germany
¹⁵Centre for Astrophysics and Supercomputing, Swinburne University of Technology, PO Box 218, Hawthorn, VIC 3122, Australia
¹⁶Staples High School, Westport CT
¹⁷Cerro Tololo Inter-American Observatory, National Optical Astronomy Observatory, Casilla 603, La Serena, Chile
¹⁸Department of Physics & Astronomy, University College London, Gower Street, London, WC1E 6BT, UK
¹⁹Department of Physics and Electronics, Rhodes University, PO Box 94, Grahamstown, 6140, South Africa
²⁰CNRS, UMR 7095, Institut d'Astrophysique de Paris, F-75014, Paris, France
²¹Sorbonne Universités, UPMC Univ Paris 06, UMR 7095, Institut d'Astrophysique de Paris, F-75014, Paris, France
²²Observatories of the Carnegie Institution of Washington, 813 Santa Barbara St., Pasadena, CA 91101, USA
²³Department of Physics, Stanford University, 382 Via Pueblo Mall, Stanford, CA 94305, USA
²⁴Laboratório Interinstitucional de e-Astronomia - LIneA,

Rua Gal. José Cristino 77, Rio de Janeiro, RJ - 20921-400, Brazil
²⁵Observatório Nacional, Rua Gal. José Cristino 77, Rio de Janeiro, RJ - 20921-400, Brazil
²⁶Institut de Física d'Altes Energies (IFAE), The Barcelona Institute of Science and Technology, Campus UAB, 08193 Bellaterra (Barcelona) Spain
²⁷Department of Physics and Astronomy, University of Pennsylvania, Philadelphia, PA 19104, USA
²⁸Department of Physics, IIT Hyderabad, Kandi, Telangana 502285, India
²⁹Jet Propulsion Laboratory, California Institute of Technology, 4800 Oak Grove Dr., Pasadena, CA 91109, USA
³⁰Department of Physics, California Institute of Technology, Pasadena, CA 91125, USA
³¹Instituto de Física Teórica UAM/CSIC, Universidad Autónoma de Madrid, 28049 Madrid, Spain
³²Institut de Ciències de l'Espai, IEEC-CSIC, Campus UAB, Carrer de Can Magrans, s/n, 08193 Bellaterra, Barcelona, Spain
³³Department of Physics, University of Michigan, Ann Arbor, MI 48109, USA
³⁴Department of Astronomy, University of Michigan, Ann Arbor, MI 48109, USA
³⁵SLAC National Accelerator Laboratory, Menlo Park, CA 94025, USA
³⁶Department of Astronomy, University of Illinois, 1002 W. Green Street, Urbana, IL 61801, USA
³⁷National Center for Supercomputing Applications, 1205 West Clark St., Urbana, IL 61801, USA
³⁸Center for Cosmology and Astro-Particle Physics, The Ohio State University, Columbus, OH 43210, USA
³⁹Department of Physics, The Ohio State University, Columbus, OH 43210, USA
⁴⁰Astronomy Department, University of Washington, Box 351580, Seattle, WA 98195, USA
⁴¹Australian Astronomical Observatory, North Ryde, NSW 2113, Australia
⁴²Departamento de Física Matemática, Instituto de Física, Universidade de São Paulo, CP 66318, CEP 05314-970, São Paulo, SP, Brazil
⁴³Instituto de Física, UFRGS, Caixa Postal 15051, Porto Alegre, RS - 91501-970, Brazil
⁴⁴Centro de Investigaciones Energéticas, Medioambientales y Tecnológicas (CIEMAT), Madrid, Spain
⁴⁵School of Physics and Astronomy, University of Southampton, Southampton, SO17 1BJ, UK
⁴⁶Instituto de Física Gleb Wataghin, Universidade Estadual de Campinas, 13083-859, Campinas, SP, Brazil
⁴⁷Computer Science and Mathematics Division, Oak Ridge National Laboratory, Oak Ridge, TN 37831